



Modulation of b-axis thickness within MFI zeolite: Correlation with variation of product diffusion and coke distribution in the methanol-to-hydrocarbons conversion



Ning Wang^{a,b,*}, Yilin Hou^{a,1}, Wenjing Sun^c, Dali Cai^a, Zhaohui Chen^a, Lingmei Liu^b, Binghui Ge^d, Ling Hu^a, Weizhong Qian^{a,*}, Fei Wei^a

^a Beijing Key Laboratory of Green Chemical Reaction Engineering and Technology, Department of Chemical Engineering, Tsinghua University, Beijing 100084, China

^b Advanced Membranes and Porous Materials Center, Physical Sciences and Engineering Division, King Abdullah University of Science and Technology (KAUST), Thuwal 23955-6900, Saudi Arabia

^c China-America Cancer Research Institute, Key Laboratory for Medical Molecular Diagnostics of Guangdong Province, Guangdong Medical University, Dongguan, Guangdong 523808, China

^d Beijing National Laboratory for Condensed Matter Physics, Institute of Physics, Chinese Academy of Sciences, Beijing 100190, China

ARTICLE INFO

Keywords:
MFI zeolite
b-axis thickness
Anisotropy
Coke formation
Methanol-to-hydrocarbons

ABSTRACT

The conversion of methanol-to-hydrocarbons (MTH) has been studied over a series of Zn/ZSM-5 zeolites with different thickness of b-axis, as well as similar lengths of a-axis. It has been demonstrated that the decrease of b-axis thickness from 220 nm to 2 nm leads to the remarkably longer lifetime, accompanied by the shift of selectivity toward trimethylbenzene and increased coke tolerance capacity. Methylbenzenes, as the intermediate product of the aromatic-based cycle, can diffuse out of the straight channels in the Zn/ZSM-5 nanosheet quickly, suppressing the aromatic-based cycle. The evolution of coke species, including the quantity, types, and location, as a function of the reaction time, has been systematically investigated. During the initial reaction period, the coke preferentially forms in mesopores and then is deposited mainly in micropores as the reaction proceeds. The Zn/ZSM-5 nanosheet shows a crystal face dependency on coke deposition, which mainly occurs on the (010) surface because the diffusion of product molecules is found to be only through the straight channels. But, for the conventional Zn/ZSM-5 catalyst, the diffusion of small molecule products is through both channels, while aromatics are only diffused through the straight channels, which leads to the significant difference of coke densities and sp^2/sp^3 ratios on the (010) and (100) surfaces. The adsorption simulations indicate that butene and p-xylene are the largest molecules which diffuse through the sinusoidal channels and the straight channels, respectively.

1. Introduction

There has been an increasing political and scientific focus on the gradual depletion of world-wide crude oil deposits and the environmental influences of the large-scale use of fossil resources, so it is necessary to develop alternative routes in order to meet the demands of the growing world population. The conversion of methanol-to-hydrocarbons (MTH) offers a plausible nonpetroleum pathway for the production of fuels and chemicals from alternative sources, such as gasoline-range hydrocarbons (methanol-to-gasoline (MTG)) [1–3], light olefins (methanol-to-olefins (MTO)) [4–6], branched alkanes [7,8],

aromatics (methanol-to-aromatics (MTA)) [9,10], and other value-added chemicals [11].

Zeolites with various pore structures are used as catalysts for MTH processes with different target products [12] because pore structure has a decisive effect on the “hydrocarbon pool” mechanism, which has received wide recognition in MTH reactions. Two distinct but dependent catalytic cycles are contained in this mechanism: the aromatic- and olefin-based cycles (Fig. 1) [13,14]. In the aromatic-based cycle, methylbenzenes (MBs) react with methylating agent (such as methanol and dimethyl ether) to form more substituted MBs, which subsequently dealkylate light olefins to complete this cycle. In the olefin-based cycle,

* Corresponding authors at: Beijing Key Laboratory of Green Chemical Reaction Engineering and Technology, Department of Chemical Engineering, Tsinghua University, Beijing 100084, China.

E-mail addresses: ning.wang.1@kaust.edu.sa (N. Wang), qianwz@tsinghua.edu.cn (W. Qian).

¹ These authors contributed equally.

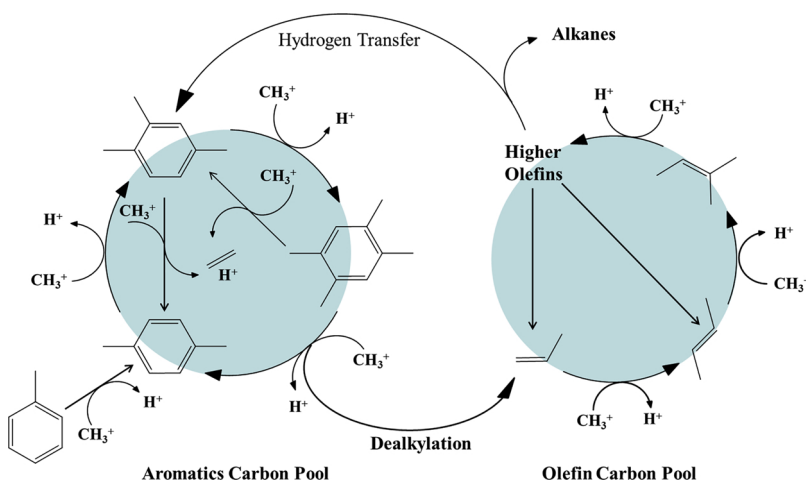


Fig. 1. Dual olefin and aromatic methylation catalytic cycle for methanol-to-hydrocarbons on ZSM-5 [13].

higher olefins are produced by olefins methylation, and subsequently either crack to form lighter olefins or form aromatics through cyclization and hydrogen transfer reaction. Both cycles are simultaneously performed inside the micropores of zeolite, and the various product distributions of MTH on different zeolites can be accounted for by the affection of zeolite pore structure on the relative propagation of these two cycles.

For example, the product over SAPO-34 is mainly light olefins because it has large 12-membered ring cavities with small pore openings which enrich aromatic intermediates, resulting in the aromatic-based cycle dominating over the olefin-based cycle [6,15,16]. In contrast, in the one-dimensional pores of ZSM-22, the aromatic-based cycle is restricted, while the olefin-based cycle dominates and leads to high selectivity for branched C_5^+ -fraction alkenes because the 10-membered ring channels are too small to form polyMBs intermediates [17]. In these two zeolites, one cycle predominantly propagates over the another; however, in other zeolites, such as ZSM-5, both cycles contribute to the product distribution which can be tuned to different extents by varying the reaction conditions, such as feed composition [18], mesoporosity [3,19,20], and zeolite crystal size [21–24], to regulate the proportion of these two cycles.

The roles of mesoporosity have been evaluated in MTH processes. For instance, zeolite microtubes with trimodal porosity were recently synthesized by our team [3]. There were sufficient intercrystalline voids in that structure so that the mass transfer of guest molecules was enhanced dramatically and a higher selectivity of aromatics and C_5 paraffin was obtained compared to its conventional analogue.

The crystallite size, as a macroscopic variable, also affects the product selectivity of MTH. Rownaghi et al. [21] compared the catalytic performance on ZSM-5 nanocrystals with those on a conventional one. The nano ZSM-5 exhibited a lower olefin selectivity (6.6%) and a higher paraffin selectivity (33.6%), both of which were attributed to the fact that ethylene and propylene were hydrogenated to ethane, propane, and higher paraffins. Recently, Bhan's group [22] studied the influence of ZSM-5 particle size on product selectivity in MTH process. They proved that larger particles enhanced the proportion of the aromatic-based cycle, which led to a higher selectivity of light olefin.

Although the roles of the crystal size of MFI zeolite involved in diffusion in the two types of pore channels have been evaluated in various hydrocarbon conversion processes [12,21–24], a question of urgent relevance, namely, the impact of each channel alone on the products (diffusion and distribution) and coke (quantity, type, and location), has never been studied. The significant diversity between the two types of channels (1D straight channels ($5.6 \times 5.4 \text{ \AA}$ in diameters, parallel to the b -axis) and 2D sinusoidal channels ($5.5 \times 5.1 \text{ \AA}$ in diameters) parallel to the a -axis [25,26]) is speculated to lead to different

catalytic performances and product distributions. The straight channels are favorable for mass transfer, while the sinusoidal channels can result in strong transport restrictions [26]. Any change in mass transfer within the zeolite crystallite can have a significant impact on the product distribution.

Our goal is to elucidate the respective roles of the two types of pore channels on the MTH catalytic properties and molecular diffusion. Here, Zn/ZSM-5 catalysts, with a b -axis thickness from 2 to 220 nm and with similar acidity, porosity, and length of a -axis, have been synthesized and investigated. In order to improve the aromatics selectivity, Zn was introduced into the zeolites. We have analyzed all products and explored the coke species and their distribution in Zn/ZSM-5 with the assistance of electron energy loss spectroscopy (EELS). The results we obtained explain the difference between the straight channels and sinusoidal channels on its catalytic properties and product diffusion and provide vital insights into the selective control of the reaction path and the acquisition of the desired product.

2. Experimental

2.1. Catalyst preparation

2.1.1. Synthesis of surfactants

The surfactants $[C_{22}H_{45}N^+(CH_3)_2-C_6H_{12}-N^+(CH_3)_2-C_6H_{13}]Br_2$ (abbreviated as $C_{22-6-6}Br_2$) were synthesized according to the procedures described in the literature [27].

The synthesis of surfactants $[C_{22}H_{45}N^+(CH_3)_2-C_6H_{12}-N^+(CH_3)_2-C_6H_{13}](OH)_2$ (abbreviated as $C_{22-6-6}(OH)_2$) was as follows: $C_{22-6-6}Br_2$ were transformed to $C_{22-6-6}(OH)_2$ through reaction with Ag_2O in deionized water. The solution containing $C_{22-6-6}Br_2$, Ag_2O , and water was stirred for 24 h at an $Ag_2O/C_{22-6-6}Br_2$ molar ratio of 1.2 at room temperature. The remaining Ag_2O powder and the $AgBr$ precipitate which formed were removed by filtration. The resultant solution contained 13 wt% $C_{22-6-6}(OH)_2$.

The surfactants $[C_{22}H_{45}N^+(CH_3)_2-C_6H_{12}-N^+(CH_3)_2-C_3H_7]Br_2$ (abbreviated as $C_{22-6-3}Br_2$) were prepared according to a previous method [28]. We first prepared $C_{22-6-3}Br$ as outlined above. Then, 56.2 g (0.10 mol) of $C_{22-6-3}Br$ and 25 g of 1-bromopropane (Aldrich, 99%) were dissolved in 100 mL acetonitrile. The solution was refluxed in an oil bath at 70 °C for 10 h. After cooling to room temperature, the white solid ($C_{22-6-3}Br_2$) was filtered, washed with diethyl ether, and dried in a vacuum oven at 50 °C.

2.1.2. Preparation of Zn/ZSM-5 catalysts with various b -axis thickness

For the preparation of ZSM-5 nanosheet (2 nm thickness), sodium silicate solution ($SiO_2/Na = 1.75$, 29 wt% SiO_2), $C_{22-6-6}Br_2$,

$\text{Al}_2(\text{SO}_4)_3 \cdot 18\text{H}_2\text{O}$, NaOH , H_2SO_4 and deionized water were mixed with $30\text{Na}_2\text{O}:1\text{Al}_2\text{O}_3:100\text{SiO}_2:10\text{C}_{22-6-6}\text{Br}_2:18\text{H}_2\text{SO}_4:4000\text{H}_2\text{O}$. The resultant gel was transferred to a Teflon-coated stainless-steel autoclave, and heated at 150°C for 5 d with the autoclave set to tumbling at 60 rpm. After crystallization, the zeolite product was filtered, washed with deionized water, and dried at 120°C . The product was calcined at 550°C for 4 h under flowing air.

For preparation of zeolite with a b-axis thickness of 10 nm, TEOS, $\text{C}_{22-6-6}(\text{OH})_2$, $\text{Al}_2(\text{SO}_4)_3 \cdot 18\text{H}_2\text{O}$, and deionized water were mixed with $100\text{SiO}_2:1\text{Al}_2\text{O}_3:15\text{C}_{22-6-6}(\text{OH})_2:3\text{H}_2\text{SO}_4:6000\text{H}_2\text{O}$. The mixture was transferred to a Teflon-coated stainless-steel autoclave, and heated at 150°C for 9 d.

Then, the Na-type zeolite was converted into H-type zeolite by cation-exchange in a NH_4NO_3 solution at 80°C for 3 times and intermediate calcination in air at 550°C for 4 h.

For the preparation of zeolites with a b-axis thickness of 60 and 220 nm, TEOS, tetrapropylammonium hydroxide (TPAOH), $\text{Al}(\text{O-i-Pr})_3$, and deionized water were mixed with $100\text{TEOS}:1\text{Al}_2\text{O}_3:x\text{TPAOH}:3700\text{H}_2\text{O}$ ($x = 0.30$ and 0.15). After stirring for 3 h at 35°C , the resultant solution was heated at 80°C in order to remove the ethanol generated during the hydrolysis of TEOS, and then deionized water was added to maintain a constant volume. After crystallization at 170°C for 3 d, the product was recovered by centrifugation and dried overnight at 120°C . Finally, the template was removed by calcination in static air at 550°C for 4 h.

The corresponding Zn/ZSM-5 with loading amount of 2 wt% were prepared by traditional incipient wetness impregnation method. The catalysts were abbreviated as Zn/Z5 (x, y) with x as b-axis thickness and y as Si/Al ratio.

2.2. Catalyst characterization

X-ray diffractions (XRD) were recorded on a Rigaku D/Max-RB diffractometer with $\text{Cu K}\alpha$ radiation at 40 kV and 120 mA.

Transmission electron microscopy (TEM) experiments were performed using a transmission electron microscope (TEM) (JEM-2010; JEOL, Tokyo, Japan), exited at 120 kV and equipped with selected area electron diffraction (SAED).

HAADF-STEM and EELS measurements were obtained with an ARM-200 TEM operated at an acceleration voltage of 200 kV (JEOL, Tokyo, Japan) and equipped with double spherical aberration (Cs) correctors.

The Si/Al ratio of the zeolite was obtained by an inductively coupled plasma optical emission spectrometer (ICP-OES) (IRIS Intrepid II XSP).

Argon physisorption was performed on an Autosorb-IQ2-MP-C system (Quantachrome Instruments, Boynton Beach, FL, USA) at -186°C . The pore size distribution was evaluated by an NLDFT method using the silica cylindrical pore, adsorption branch model.

^{27}Al and ^{29}Si MAS NMR experiments were performed on a Bruker AVANCE III 600 spectrometer at resonance frequencies of 156.4 MHz and 119.2 MHz, respectively. ^{27}Al MAS NMR spectra were recorded on a 4 mm probe by the small-flip angle technique with a pulse length of $0.5\ \mu\text{s}$ ($<\pi/12$) and a 1-s recycle delay. ^{29}Si MAS NMR spectra with high-power proton decoupling were recorded on a 4 mm probe with a spinning rate of 12 kHz, a $\pi/4$ pulse length of $2.6\ \mu\text{s}$, and a recycle delay of 80 s. The chemical shifts of ^{29}Si and ^{27}Al were referenced to TMS and 1 mol/L aqueous $\text{Al}(\text{NO}_3)_3$, respectively.

NH_3 -TPD analysis was completed in a Quantachrome automated chemisorption analyzer from room temperature to 850°C with a ramp of $10^\circ\text{C}/\text{min}$.

Brønsted and Lewis acid sites were determined by pyridine adsorption. The samples were first dried, in situ, by heating to 450°C under vacuum and then cooled to 50°C . At this temperature, the samples were exposed to pyridine vapor using an equilibration time of 30 min. After the physically adsorbed pyridine molecules were removed by outgassing at 150°C for 1 h, infrared (IR) spectra were collected at

150°C with $4\ \text{cm}^{-1}$ resolution using a Nicolet FTIR spectrometer.

Thermogravimetric analysis (TGA) was carried out using a thermogravimetric analyzer (TGA/DSC-1) from 30 to 900°C at a heating rate of $10^\circ\text{C}\ \text{min}^{-1}$ in air.

UV-Raman spectra of the spent Zn/Z5 catalysts were recorded using an excitation wavelength of 325 nm on a Renishaw (RM2000) spectrometer.

All of the adsorption simulations in the present study were carried out using the Materials Studio simulation package (Accelrys Software). The adsorption of product molecules in MFI were determined using the grand canonical Monte Carlo (GCMC) simulation method. The partial charges of atoms were estimated by the charge-equilibration method, and electrostatic energy was calculated by the Ewald summation method, which is highly accurate in the long range interactions calculation. The metropolis scheme was used at a constant pressure and temperature. The average loading was 30 molecules so that we could obtain statistically reliable results.

The Ewald summation technique with a Ewald accuracy of 1×10^{-5} kcal/mol was used for the electrostatic potential energy. For achieving equilibration, 2×10^6 Monte Carlo steps were carried out, and, for the calculation of the required properties and the data analysis 1×10^6 , additional steps were used.

In all calculations, the zeolite framework was treated as a rigid structure. The simulation box is a super cell which is large enough to obey the minimum image convention. The super cell consisted of 27 unit cells ($3 \times 3 \times 3$, $a = 60.06\ \text{\AA}$, $b = 59.69\ \text{\AA}$, and $c = 40.15\ \text{\AA}$). Periodic boundary conditions were applied in all directions.

2.3. Catalyst evaluation: methanol-to-hydrocarbons reaction

The catalytic tests were performed at the conditions of 1 atm, 475°C , and $\text{WHSV} = 0.8\ \text{h}^{-1}$ (under N_2 flow ($10\ \text{mL}\ \text{min}^{-1}$ controlled by mass flowmeter) in a conventional fixed bed quartz reactor (13.0 mm i.d.), equipped with a thermocouple in the middle of the catalyst bed. The 0.5 g catalyst was placed in the middle of the reactor. The flow rate of pure methanol was controlled by a dual micro-plunger pump.

The products were analyzed using an online gas chromatograph (Shimadzu GC-2014; Shimadzu, Tokyo, Japan) equipped with three separate columns and detectors. A thermal conductivity detector (TCD) coupled with a Molsieve 5 Å column was used to analyze light gases (H_2 , N_2 , CH_4 , and CO). $\text{C}_1 - \text{C}_4$, C_{5+} and aliphatics were analyzed using an FID on an MC-3 column, and aromatics were analyzed using an FID on an MC-4 column.

The methanol conversion and selectivity of the products were calculated from the number of C atoms with the following formula:

$$\text{Conversion (C}_{\text{mol}\%}\text{)} = (1 - \text{A}_{\text{MeOH}}\text{RF}_{\text{MeOH}} / (\sum A_i\text{RF}_i + \text{A}_{\text{MeOH}}\text{RF}_{\text{MeOH}})) \times 100\%$$

$$\text{Selectivity}_i (\text{C}_{\text{mol}\%}) = A_i\text{RF}_i / (\sum A_i\text{RF}_i) \times 100\%,$$

where A_i represents the peak area and RF_i represents the response factor for GC of component i .

3. Results and discussion

3.1. Catalyst characterization

The as-synthesized Zn/Z5 zeolite catalysts with various b-axis thickness are shown in Fig. 2. The Z5 (2, 50) and Z5 (10, 50) have flake-like morphology, which is composed of three dimensionally intergrown nanosheets (Fig. 2a and d). The $\text{C}_{22-6-6}\text{N}_2\text{Br}_2$ -templated zeolite nanosheet is composed of a discrete MFI layer with a single-unit-cell thickness (three pentasil sheets) (Fig. 2a and b, Fig. S1a–f). It was found that the crystallization of MFI zeolite gel at Si/Al ratio of 25 using $\text{C}_{22-6-6}\text{N}_2\text{Br}_2$ as a structure-directing agent (SDA) results in an

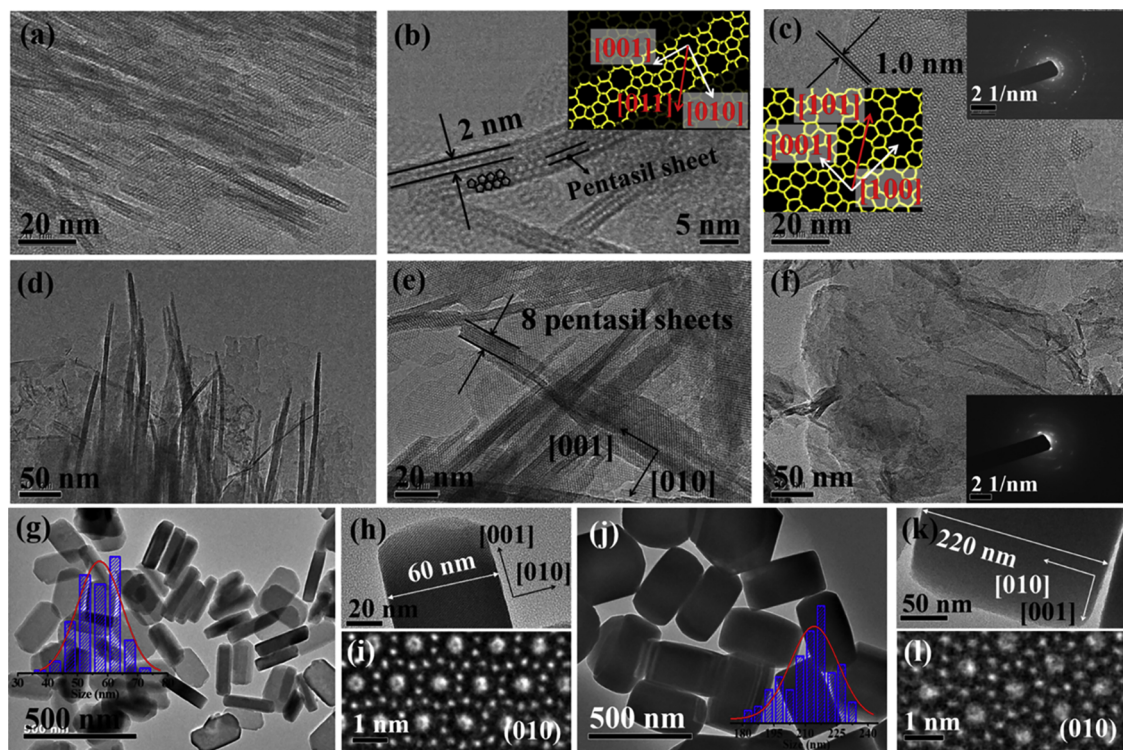


Fig. 2. TEM images of Zn/Z5 zeolites with various b-axis thickness: (a–c) Zn/Z5 (2, 50), (d–f) Zn/Z5 (10, 50), (g–i) Zn/Z5 (60, 50), and (j–l) Zn/Z5 (220, 50).

amorphous product (Fig. S1g and h). Here, by using propyl instead of the hexyl end group, highly crystalline MFI zeolite with Si/Al ratio of 25 can be obtained because increased occupancy of the intersections of the zeolite framework by quaternary ammonium centers increases the crystallization rate (Fig. S1i and j) [28].

When $C_{22-6-6}N_2(OH)_2$ is used as the SDA, the thickness of the Zn/Z5 nanosheet increases to 8–12 pentasil layers, with an average b-axis thickness of 10 nm (Fig. 2d and e). Fig. 2c and f reveal that the zeolite nanosheets have large coherent domains along the a–c planes of the plate. Zn/Z5 (60, 50) and Zn/Z5 (220, 50) have regular crystal morphology and uniform dispersion (Fig. 2g and j). The mean b-axis thickness, measured by averaging the sizes of 100 primary particles, are 60 nm (Fig. 2g and h) and 220 nm (Fig. 2j and k) for Zn/Z5 (60, 50) and Zn/Z5 (220, 50), respectively. The straight channels of zeolites can be distinguished in all of the samples (Fig. 2f, i, and l). Although the b-axis thickness shows great differences, these MFI zeolites have similar a-axis lengths, estimated to be ~ 320 nm (Fig. S2).

The Ar physisorption isotherms of the Zn/Z5 zeolite catalysts are shown in Fig. S3a. The Zn/Z5 nanosheets (b-axis thickness of 2 and 10 nm) and Zn/Z5 (60, 50) combine the characteristics of type I and type IV shaped isotherms, consistent with their predominantly mesoporous nature. The isotherms of Zn/Z5 (220, 50) are of type I, in line with the predominance of micropores. Compared to Zn/Z5 (10, 50), Zn/Z5 (2, 50) shows more mesopores formed by the arrangement of the nanosheets, as proven by the more obvious step in the Ar uptake. The mesopore diameters (NLDFT method) in these samples have a narrow distribution ranging from 3 to 7 nm (Fig. S3b). As shown in Table 1, although the micropore volumes of the nanosheet zeolites are lower than those of the conventional zeolites, the nanosheets have much higher mesopore volumes (0.79 – 0.97 cm^3/g) and surface areas (480 – 545 m^2/g).

XRD patterns (Fig. S3c) show that the positions of the diffraction peaks of the zeolite nanosheets are in line with those of the conventional zeolites. Only the $h0l$ reflections are sufficiently sharp for indexing because the zeolite nanosheet possesses wide a–c planes having large coherent domains [29]. There is no diffraction peak of ZnO in the

XRD patterns, and the ZnO nanoparticles (NPs) are not observed in TEM images (Fig. 2), indicating highly dispersed ZnO NPs in the MFI zeolite. The ^{27}Al MAS NMR spectra of all the samples (Fig. S3d) show only one sharp and symmetrical signal at 55 ppm, indicating that all the aluminum atoms are incorporated into the MFI framework with a tetrahedral coordination environment [30–32].

The NH_3 -TPD curves (Fig. 3a) and pyridine-absorbed FTIR spectra (Fig. 3b) show that there are minor differences among the Zn/Z5 (x, 50) zeolite catalysts with various b-axis thickness because of their similar Si/Al ratio. As shown in the NH_3 -TPD spectra (Fig. 3a), two NH_3 desorption peaks, namely, low temperature and high temperature peaks, are observed at approximately 250 and 370 $^\circ\text{C}$, respectively. It can be seen that the amount and strength of acid sites over Zn/Z5 (x, 50) catalysts were all similar. In the case of Zn/Z5 (2, y) catalysts, the acid amount declines sharply with the increasing Si/Al ratio. From the Py-FTIR spectra (Fig. 3b), the peaks at 1445 and 1540 cm^{-1} are representative of Lewis and Brønsted acid sites, respectively, and the peak at 1490 cm^{-1} represents both Lewis and Brønsted acid sites [33]. It is also noteworthy that the amount of Lewis acid decreases significantly with increasing Si/Al ratio.

3.2. Catalytic performances of Zn/Z5 catalysts with different b-axis thickness

The critical impact of b-axis thickness on the catalytic stability of the MFI is revealed in the MTH reaction. As expected, the Zn/Z5 (2, 50) shows the slowest deactivation (defined as the time at which the catalytic conversion decreases by 50%, which is abbreviated as $t_{0.5}$) of more than 190 h, which is almost 60-fold that of Zn/Z5 (220, 50) ($t_{0.5} = 3$ h) (Fig. 4). For these samples with different Si/Al ratios, the acidity is the main factor which is responsible for the difference in the catalyst lifetimes [34]. With increasing b-axis thickness, the lifetimes of Zn/Z5 catalysts exhibit a descending trend. Given that four Zn/Z5 (x, 50) catalysts have identical framework types, similar acid sites (strength and amount) (Fig. 3), and comparable a-axis lengths (Fig. S2), the significant difference of catalytic performance among these catalysts

Table 1

Textural properties of various Zn/Z5 zeolites catalysts.

Catalysts	Si/Al ^a	S _{BET} (m ² /g)	V _{total} (cm ³ /g) ^b	V _{micro} (cm ³ /g) ^b	V _{meso} (cm ³ /g) ^b	S _{micro} (m ² /g) ^c	S _{external} (m ² /g) ^c
Zn/Z5 (2, 25)	26.1	480.0	0.863	0.065	0.798	190.0	290
Zn/Z5 (2, 50)	54.2	545.8	1.050	0.072	0.978	301.5	244.3
Zn/Z5 (2, 80)	85.6	532.7	0.902	0.079	0.823	316.9	215.8
Zn/Z5 (10, 50)	52.6	491.0	0.938	0.158	0.780	405.4	85.6
Zn/Z5 (60, 50)	51.4	460.8	0.687	0.204	0.483	423.2	37.6
Zn/Z5 (220, 50)	51.7	435.8	0.251	0.158	0.093	418.4	17.4

^a Si/Al atomic ratios measured by ICP-OES.^b Pore volume determined via the NLDFT method.^c Estimated by the t-plot method.

can be directly attributed to the b-axis thickness. Moreover, the catalytic performance is significantly affected by Si/Al ratios. Among these three catalysts, the Zn/Z5 (2, 25) sample shows much lower stability ($t_{0.5} = 22$ h). This behavior can be attributed to the highest number of acid sites [34]. While the Zn/Z5 (2, 80) sample shows excellent stability ($t_{0.5} = 174$ h), but slightly lower than that of Zn/Z5 (2, 50) (197 h). Actually, in our previous work, similar phenomena have been observed [9]. According to our previous results [9], that is because more C_{9+} benzene can be formed over Zn/Z5 (2, 80) compared to Zn/Z5 (2, 50), which can cause micropore blockage more easily over Zn/Z5 (2, 80).

By using a model proposed by Janssens [35], the conversion capacity (R), the rate constant (k), and the deactivation coefficient (α) are derived from the stability plots. The calculated results (Table S2) show that, with increasing b-axis thickness, the conversion capacity R (from 157.63 to 2.77 g_{MeOH}g_{cat}⁻¹) drops, while α increases (from 0.203 to 11.527 g_{cat}mol_{MeOH}⁻¹). The unit cell thickness along the b-axis within Zn/Z5 (2, 50) catalyst allows all acid sites to be easily accessible through the straight channels and, thus, shows a higher conversion rate and a larger conversion capacity. At the same time, it suppresses the coke formation (by fast diffusion and mass transfer in the straight channels) and enhances the coke tolerance capacity, which explains the longer catalytic lifetime. The slightly lower stability of Zn/Z5 (10, 50) (compared to Zn/Z5 (2, 50)) is due to the higher internal concentration of acid sites and diffusional resistance, reducing the overall reaction rate. In obvious contrast, the severe diffusion limitations on Zn/Z5 (220, 50) can cause pathway blockage to the active sites inside the micropores for reacting molecules, resulting in rapid deactivation of the catalyst.

We have observed the alterations of product (i.e., alkene, aromatics, and alkane) selectivity on Zn/Z5 zeolites with TOS, as shown in Fig. 5 and Fig. S4, until the catalysts are essentially deactivated (conversion < 50%). In the case of Zn/Z5 (220, 50), xylene and C₂-C₄ alkane initially are the main products, reflecting exhaustive hydrogen transfer.

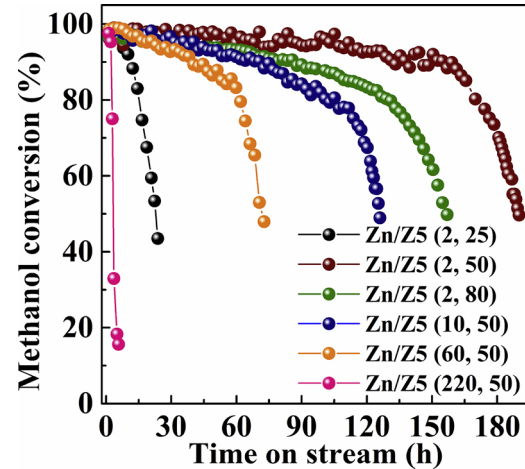


Fig. 4. Methanol conversions on Zn/Z5 as a function of time on stream (reaction temperature: 475 °C; reaction pressure: atmospheric pressure, WHSV: 0.8 h⁻¹).

With the progress of the reaction, olefins and methane gradually increase. Finally, methane selectivity increases to about 25%, suggesting the dehydrogenation of coke on the surface with methanol [36] (Scheme 1).

The other three catalysts give TriMBs as the main products (1,2,4-TriMBs dominating in this fraction, Table S3) at the beginning of the reaction (Fig. 5f), but their selectivity gradually decreases as the reaction proceeds, while the selectivity of toluene and xylene increases, and then levels off (Fig. 5d and e). Our previous study has verified that TriMBs are rarely formed in the pores of the MFI zeolite [33], so the formation of TriMBs only occurs on the external surface of the MFI zeolite through the alkylation of xylene. In the initial stage of the

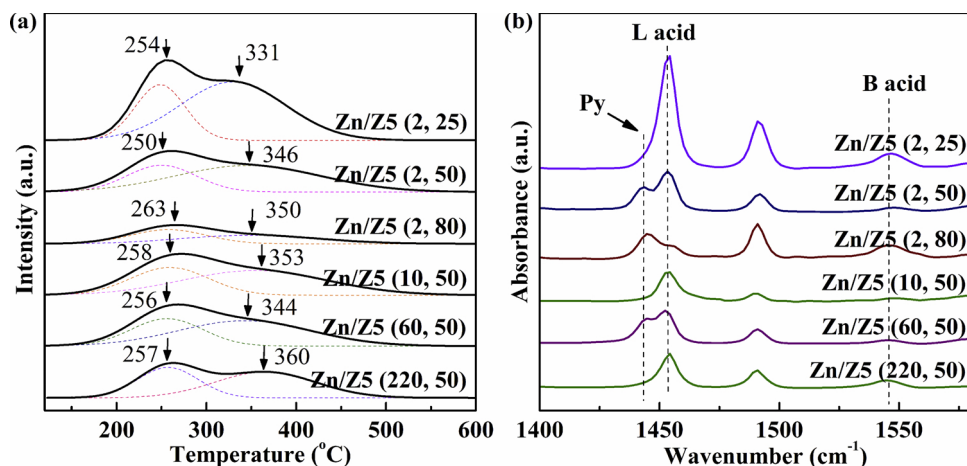


Fig. 3. (a) NH₃-TPD and (b) Py-FTIR spectra of various Zn/Z5 zeolite catalysts.

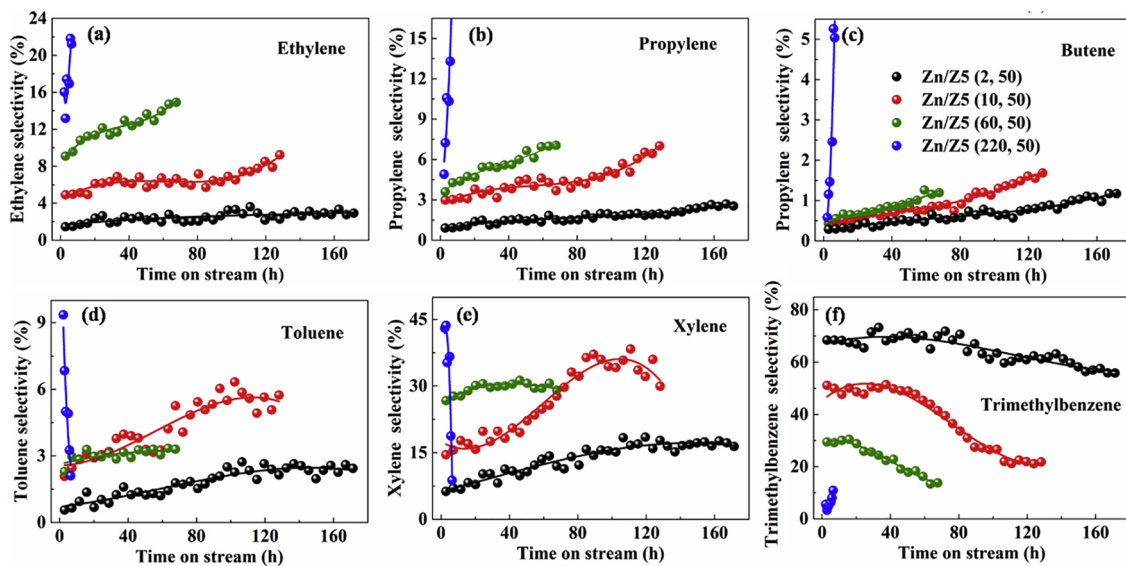
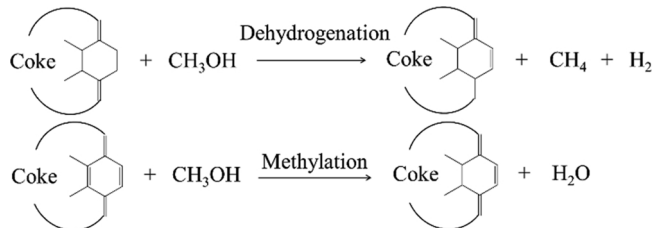


Fig. 5. Evolution of (a–c) olefin and (d–f) aromatic selectivity during the MTH conversion reaction over Zn/Z5 zeolites.



Further isomerization- and cyclization reactions

Scheme 1. The dehydrogenation of coke on the surface with methanol [36].

reaction, a high selectivity of TriMBs is obtained because a large amount of xylene is consumed and alkylated to form TriMBs in the effect of acid sites locating on the external surface of MFI zeolite. As the reaction proceeds, an increasing number of acidic sites on the external surface are covered by deposited coke; consequently, there are fewer active sites for alkylation reaction. Thus, the selectivity of toluene and xylene level off when the external surface of the zeolite is completely covered by carbon deposition.

In addition, methane selectivity over these three catalysts declines in the first half and then increases in the latter half of the reaction process (Fig. S4a). Methane is mainly formed from the dealkylation reaction of MBs. In the initial stages of the reaction, strong acidity leads to the dealkylation reaction of MBs, forming large amounts of methane. As the reaction proceeds, more and more acid sites (mainly Brønsted acid sites) are covered by carbon deposits, resulting in a sharp decline of methane selectivity. Afterward, the cyclization dehydrogenation capacity of olefin reduces due to weakening of Lewis acid, while the hydrogen transfer and hydrogenation of olefins simultaneously increase. In addition, the formed coke can dehydrogenate on the surface with methanol. These reactions lead to the production of more methane in the latter stage of the reaction.

The alkene selectivity increases monotonically with TOS over all of the samples (Fig. 5a–c), while light paraffin (C_2 – C_4) selectivity gradually declines or remains constant (Fig. S4b–d). Certain marked differences in selectivity are evident among various catalysts. As illustrated in Table 2, ethylene selectivity increases from 1.56% to 16.82%, while propylene selectivity increases substantially and monotonically from 0.96% to 5.14% with the increasing b-axis thickness from 2 nm to 220 nm. Hence, the total light olefins selectivity increases from 2.83% (Zn/Z5 (2, 50)) to 22.57% (Zn/Z5 (220, 50)) (Table 2). Abbot and Wojciechowski [37] found that the cracking of linear olefins hardly

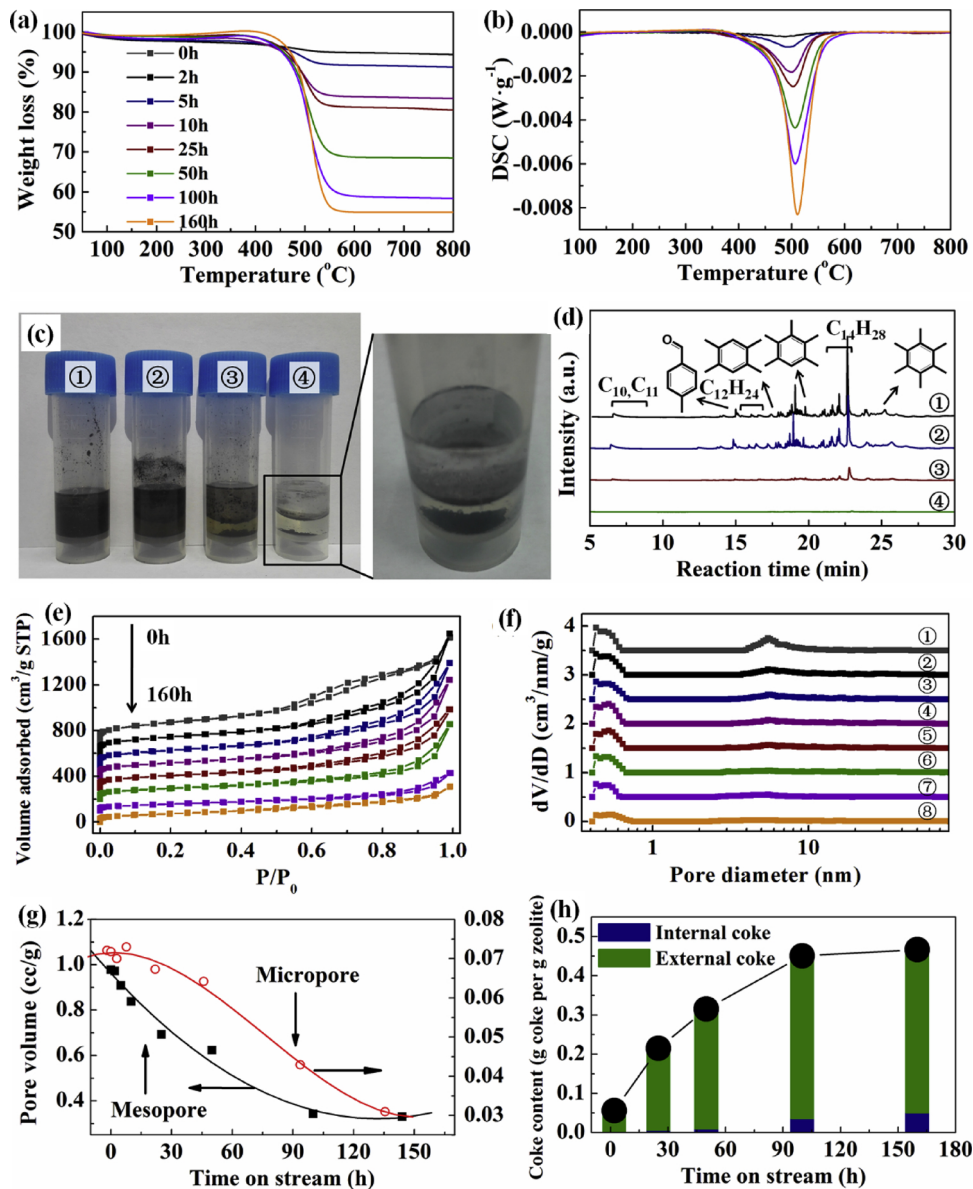
produces ethylene on MFI zeolite, suggesting that ethylene is mainly generated from the aromatics-based cycle. Besides, propylene is produced from both catalytic cycles. Thus, the relatively higher ethene selectivity with increasing b-axis thickness implies that the proportion of the aromatic-based cycle is promoted, while the olefin-based cycle is suppressed. Specifically, longer b-axis thickness in Zn/Z5 (60, 50) and Zn/Z5 (220, 50) samples can result in an increase of the residence time of MBs within the MFI crystal, so these aromatics can interact with more Brønsted acid sites and repeatedly approach to methylation/dealkylation process to produce more light olefin (ethene or propene) molecules before escaping from the pore channels [22]. In the case of the Zn/Z5 (2, 50) samples, once the MBs is formed, it is easy to escape from the straight channel of Zn/Z5 (2, 50) without undergoing further dealkylation process, and then undergo methylation process at the external surface of MFI zeolite to form higher MBs (Fig. 5f and Table 2). As shown in Table 2, with increasing b-axis thickness, the selectivity of 2MBu (the sum of 2-methylbutane and 2-methyl-2-butene), which is mainly produced from the olefin-based cycle decreases, while the light olefin selectivity and ethene/2MBu ratio increases, also indicating that the proportion of the aromatic-based cycle is enhanced while that of the olefin-based cycle is suppressed [22].

MBs are the major group of compounds retained within the pores of MFI zeolite after the MTH reaction. From Fig. 5d–f and Table 2, it can be seen that the distribution of MBs shift toward MBs with fewer methyl substituents with increasing the b-axis thickness. Zn/Z5 (2, 50) and Zn/Z5 (10, 50) contain a mixture of MBs (TriMBs > xylene > toluene) and poly-aromatic species. In contrast, Zn/Z5 (220, 50) possesses a different amount of MBs (xylene > TriMBs ≈ toluene) and the absence of poly-aromatic species after MTH reaction. From Table 2, it can be observed that the average methyl substitution in MBs reduces from 2.89 to 1.70 with increasing b-axis thickness from 2 nm to 220 nm. This is because the greater mass transfer limitation inside the micropore channels with longer b-axis prevents MBs with more methyl substituents from escaping from the micropore channels, thus reducing their relative content in the product molecules. In contrast, due to the shorter b-axis thickness and enlarged external surface area of Zn/Z5 (2, 50), the isomerization reaction of TriMBs can readily achieve dynamic equilibrium, leading to a higher selectivity of 1,2,4-TriMBs (57.3%, shown in Table S3). Consequently, the cost and energy consumption of the subsequent separation and purification can be significantly reduced to obtain high purity 1,2,4-TriMBs compared with the previous results in MTH reaction.

Table 2

Selectivity toward ethene, propene, 2MBu, and Ethene/2MBu for the MTH reaction over Zn/Z5 samples with different b-axis thickness.

Samples	Ethene	Propene	Light olefins (ethene + propene)	2MBu ^a	Ethene/2MBu ^b	Average number of methyl substituents in MBs ^c
Zn/Z5 (2, 50)	1.56	0.96	2.52	6.5	0.24	2.89
Zn/Z5 (10, 50)	5.62	3.42	9.04	6.1	0.92	2.70
Zn/Z5 (60, 50)	10.91	4.88	15.79	5.1	2.14	2.30
Zn/Z5 (220, 50)	16.82	5.14	21.96	4.6	3.66	1.70

^a 2MBu = 2-methylbutane + 2-methyl-2-butene.^b Ethene/2MBu is the ratio of the synthesis rates of ethene and 2MBu, a descriptor to reflect the relative propagation of aromatics-based cycle and olefins-based cycle.^c Average number of methyl substituents in MBs in the reaction effluent of methanol conversion over Zn/Z5 samples with different b-axis thickness at 2.8 h time on stream.**Fig. 6.** The evolution (quantity, types, and location) of coke species over spent Zn/Z5 (2, 50) catalysts with different TOS: (a) TG and (b) DSC profiles; (c) photographs after being dissolved in 20% HF and extracted by CH₂Cl₂; (d) GC-MS chromatograms of the organic species extracted by CH₂Cl₂: ① 25 h, ② 50 h, ③ 100 h, and ④ 160 h; (e) Ar physisorption isotherms and (f) the corresponding NLDFT pore size distributions; (g) evolution of pore volume; and (h) coke deposition during the MTA reaction.

3.3. Evolution of coke species (quantity, types, and location) during MTH reaction

In order to further explain their catalytic behaviors, we have

monitored the quantity and types of coke species formed during the reaction. As shown in Fig. S5a, the Zn/Z5 (2, 50) exhibits not only a higher tolerance capacity to coke than Zn/Z5 (220, 50) (467 versus 119 mg g_{cat}⁻¹), but also a much slower coke deposition than Zn/Z5

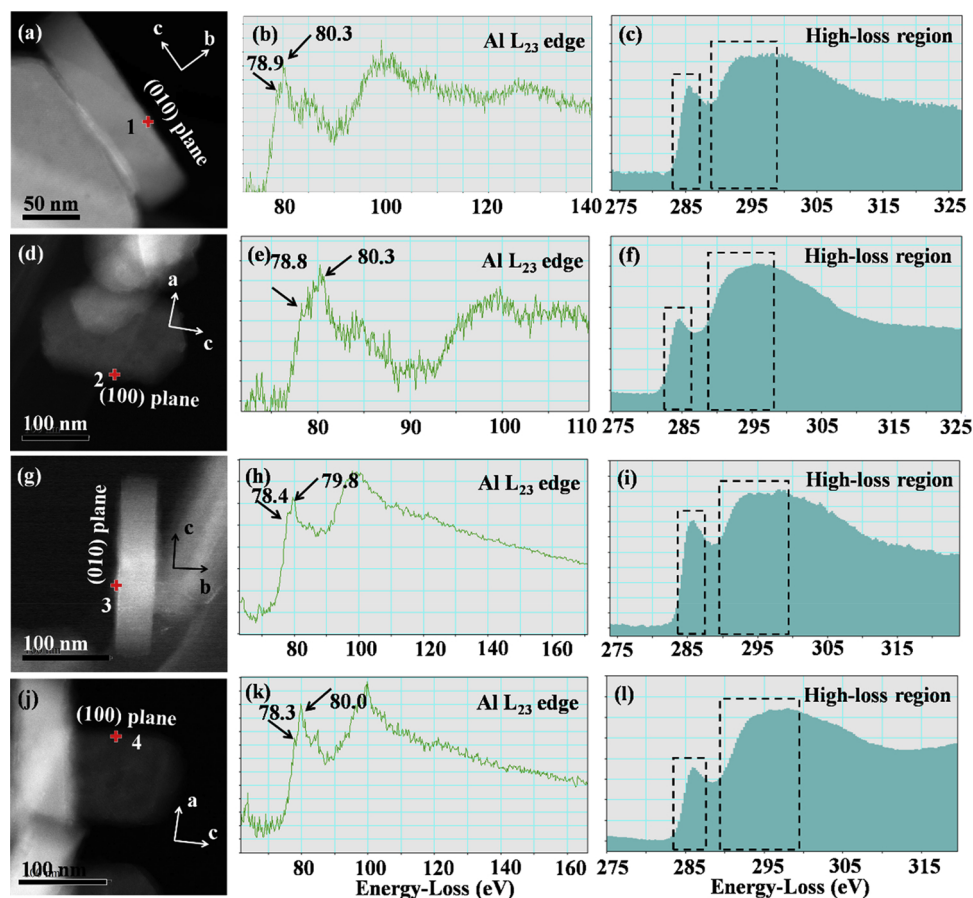


Fig. 7. HAADF-STEM images of Zn/Z5 (60, 50) after reaction: (a,d) 16 h and (g,j) 64 h; (b,e,h,k) the Al L_{2,3}-edge EELS spectra from sites 1–4 in.(a,d,g,j); (c,f,i,l) C K-edge EELS spectra collected from sites 1–4 in.(a,d,g,j).

(220, 50) (2.45 versus 39.6 mg g_{cat}⁻¹ h⁻¹). Raman spectra of spent catalysts (Fig. S5b) show that all the samples have two profiles with a D band (1347 cm⁻¹) and a G band (1575 cm⁻¹), suggesting that both amorphous carbon and graphite are formed during the reaction.

In addition, we also studied the evolution of coke species, including the quantity, types, and location, with TOS over Zn/Z5 (2, 50) catalysts. From the TG/DSC profiles (Fig. 6a and b), the reaction temperatures at which the maximum combustion rate of coke occurred shifts to higher values (from 500 °C to 550 °C) with longer TOS values. This temperature shift indicates a higher degree of condensation of coke with increasing TOS. After being treated by 20% hydrofluoric acid and extracted by CH₂Cl₂ (Fig. 6c), the GC-MS chromatograms of the organic species in spent catalysts (Fig. 6d) show that, during the initial reaction, the polycyclic aromatic hydrocarbon is mainly formed, while, as the reaction proceeded, these polycyclic aromatic hydrocarbons gradually transform into granulated graphite carbon species, which can be clearly seen from the bottom in Fig. 6c. Rojo-Gama et al. [38] also reported the accumulation of coke species which are insoluble in CH₂Cl₂ on the external surface of ZSM-5 crystals, which is consistent with our results.

As exhibited in Fig. 6e–g, the changes in the textural properties of Zn/Z5 (2, 50) catalysts are dependent on the coke content and the locations. During the initial reaction period, the coke on Zn/Z5 (2, 50) is preferentially formed in mesopores (external coke) (Fig. 6h), as evidenced by a sharp decline of mesopore distribution and volume in the first 45 h. The external coke is barely able to completely block the pore channels, and the products can still diffuse to active sites and exit the pore channels, which is verified by the TEM images of the graphite carbon below. In contrast, in the latter half of the reaction process, micropore volume significantly decreases, indicating that coke forms mainly in micropores (Fig. 6g and h).

Using STEM-EDS, we have probed the position of coke on deactivated Zn/Z5 (2, 50) and Zn/Z5 (60, 50). The coke residues are mainly deposited on the (010) surface and are rare on the (100) surface of Zn/Z5 (2, 50) (Fig. S6a), while the coke distributes much more uniformly on Zn/Z5 (60, 50) throughout the entire crystal (Fig. S6b and c). For further confirmation of the crystal face dependency for coke on Zn/Z5 (2, 50), the used samples are treated using a 20% hydrofluoric acid to remove the zeolite and also studied by TEM. The graphite nanosheet are intergrown with the lamellae arranged perpendicular to each other (Fig. S7a and b). The edges are open-ended, which further proves that the (010) surface is preferential to deposit coke prior to the (100) surface on zeolite nanosheet (Fig. S7c). The coke location over the Zn/Z5 (2, 50) catalyst with TOS is shown in detail in Fig. S8. After 10 h, coke cannot be found in either the (100) surface or the (010) surface (Fig. S8a and b). As the reaction proceeds, the coke is still not observed in the (100) surface (Fig. S8c), but in the (010) surface it is deposited with a clear layered graphitic carbon structure at a typical distance value of graphite (0.34 nm) (Fig. S8d) [39]. After 160 h of the reaction, the sinusoidal pore openings are still clearly visible with no coke deposition (Fig. S8e). In stark contrast, the (010) surface has been completely covered with coke deposition, with no straight pore mouths observed (Fig. S8f). However, in the case of Zn/Z5 (60, 50), cubic hollow carbon forms on the external surface (Fig. S7d) with ~14 nm thickness in the (010) surface (Fig. S7e) and ~10 nm thickness in the (100) surface (Fig. S7f).

By using high-resolution EELS, the deposited coke species at various locations is investigated (Fig. S9). A π -plasmon peak (~5 eV) can be found, which is a characteristic feature for graphite and related materials, and its intensity is associated with the number of unsaturated bonds [40]. The bulk plasmon peak between 22–25 eV is related to the

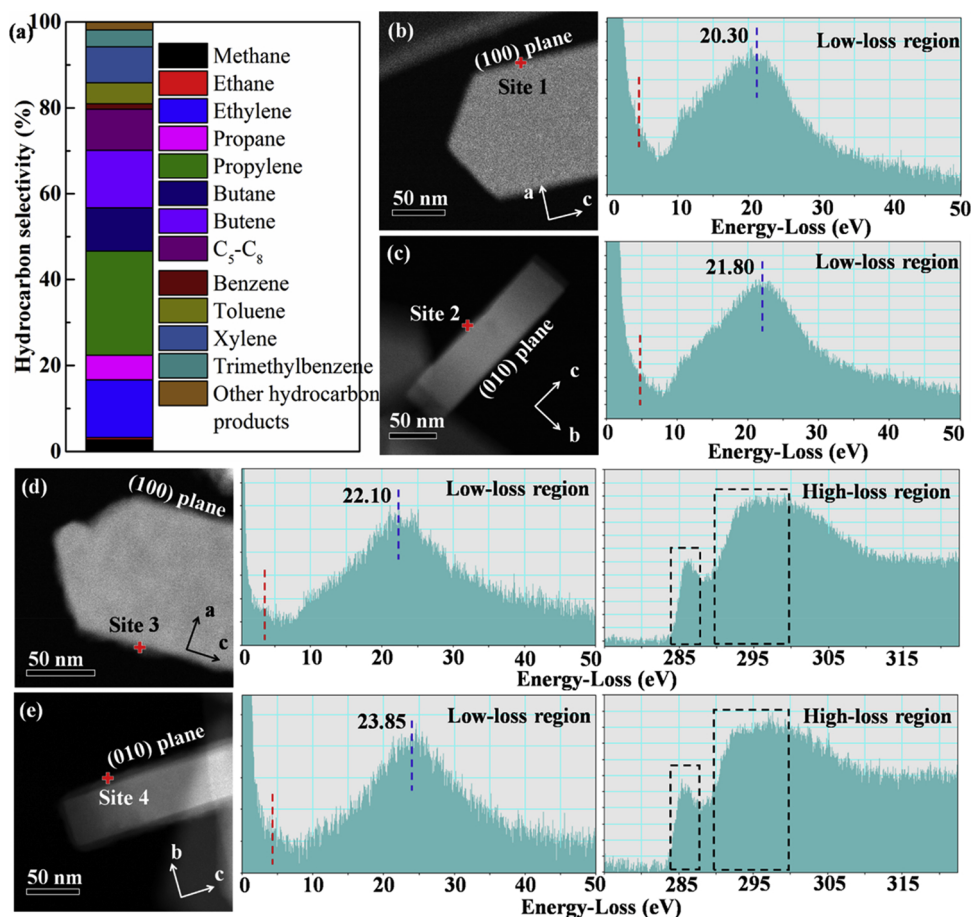


Fig. 8. (a) Product selectivity (on a C basis) of MTH reaction over ZSM-5 (60, 50) (reaction temperature: 475 °C; reaction pressure: atmospheric pressure; WHSV: 0.8 h⁻¹; the sampling time: 2.8 h); HAADF-STEM images of spent ZSM-5 (60, 50) after reaction: (b,c) 16 h and (d,e) 64 h; EELS spectra are displayed on the right.

$\sigma + \pi$ valence electron density. The coke deposited on the (010) surface (site 1) is much closer to that of the graphite at ~26 eV, compared to that on the (100) surface (site 2) (Fig. S9b and d). The densities of the coke on the (010) surface, calculated from bulk plasmon peak (formula is shown in Supporting Information), are 1.83 g/cm³, much higher than that on the (100) surface (1.45 g/cm³), suggesting much more compact lamellar structures [41].

3.4. Reason for difference of coke species on (010) and (100) surfaces

What causes such an interesting result? It may be one of the following: difference of acid sites on the external surface, difference of distribution of Zn species, or anisotropy of the micropore channel. First, the diversity of acid sites on various surface are investigated. EDX analysis of spent Zn/Z5 (60, 50) (Fig. S10a and b) prove the relatively uniform distribution of aluminum in zeolite crystals, as well as Si and O elements. According to a recent study by Schmidt et al. [42], during the MTH reaction on the ZSM-5 zeolite, the first deactivating coke precursor species forms in nanoscopic regions enriched in aluminum. Thus, in order to better connect the Al and C spectra, using the Al L₂₃-edge and C K-edge EELS spectra, we have further explored the evolution of Al species and coke species on different surfaces of Zn/Z5 (60, 50) with TOS (Fig. 7). In the C K-edge EELS spectra (Fig. 7c vs f and i vs l), by integrating the intensity over the 4 eV window (284–288 eV) and the 10 eV window (290–300 eV) (two-window method) [41], the relative sp² content is calculated. Site 1 (90.0%) and site 3 (91.0%) show higher relative sp² content than site 2 (80.0%) and site 4 (81.6%), respectively, indicating that the coke on the (010) surface has a higher degree of graphitization than that on the (100) surface, independent of reaction

time. From Fig. 7b and e, it can be found that the two surfaces have a peak of the Al L₂₃-edge which consists of a main peak at about 80 eV and a bump at the threshold region from 78 eV to 79 eV. After a reaction of 64 h, the EELS spectra of both two surfaces are quite similar, except that the positions of the shoulder peak slightly shift (Fig. 7h and k). As the EELS spectra are, in essence, XPS spectra, the shape and position of which reflect the chemical environment of each element, these results suggest that Al species on both the (101) and (100) surfaces have an extremely similar chemical bonding nature; therefore, the comparable external reaction can occur on different surfaces, and the local structure around Al after a reaction of 64 h does not change significantly from that which follows a reaction of 16 h.

Secondly, the Zn modification, which may render inhomogeneous distribution in the zeolite particles, also has a significant impact on the MTH performance [43]. In order to completely eliminate the impact of the Zn modification, we use the Z5 (60, 50) without Zn modification for the MTH reaction, and then analyze the types and location of coke species with TOS. The product distributions are shown in Fig. 8a. Compared to Zn/Z5 (60, 50), Z5 (60, 50) without introducing Zn exhibits significantly different product distribution with only 14.5% BTX, 19.0% C₁–C₄ alkanes, 51.1% C₂–C₄ olefins, and 3.9% C₉₊ aromatics. However, the EELS results of spent Z5 (60, 50) still show a significantly different graphitization degree of coke residues between the (100) surface and (010) surface (Fig. 8b–e). From the EELS spectra (Fig. 8d and e), the calculated relative sp² contents are approximately 84.0% and 76.8% for coke on the (010) surface and (100) surface, respectively. This difference between the (010) surface and (100) surface are similar to those on spent Zn/Z5 (60, 50), indicating that the Zn modification is not the cause of coke differences between the (010) surface

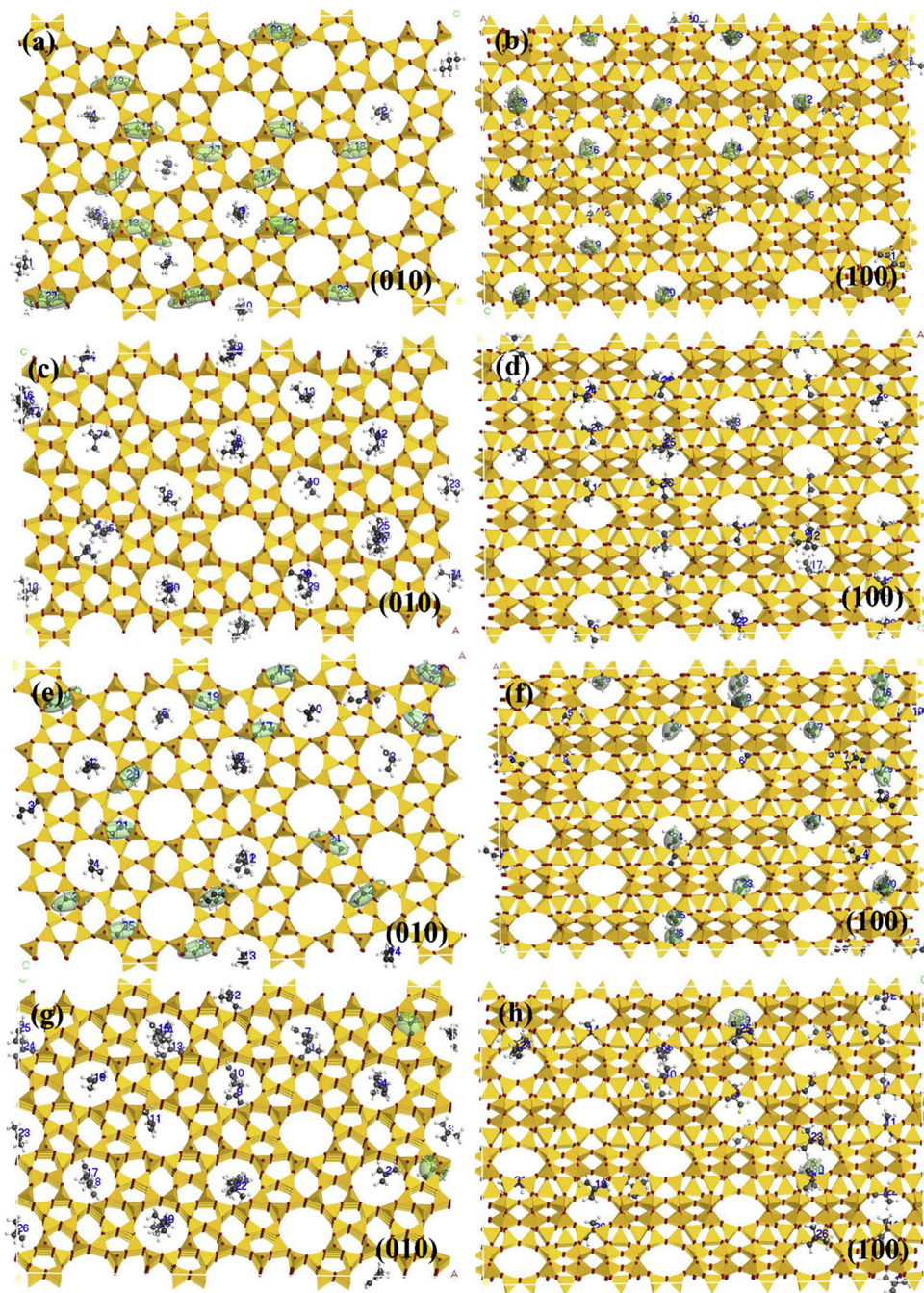


Fig. 9. The optimized location of (a,b) n-butane, (c,d) isobutene, (e,f) butane, and (g,h) isobutene molecules along the straight and sinusoidal channels of the MFI zeolite.

and (100) surface. In the low-loss EELS spectra (Fig. 8d and e), the coke deposited on the (010) surface (site 4) is at ~ 23.85 eV, much closer to that of graphite at ~ 26 eV, compared to that on the (100) surface (site 3) (~ 22.10 eV). According to the literature [41], the positions of plasmon peaks are more sensitive to structure variations compared to the high-loss spectra. Also, the intermediate coke species on Z5 (60, 50) after a reaction of 16 h show the crystal-surface difference, although they have lower degrees of graphitization (Fig. 8b and c). Thus, although the introduction of Zn has a large influence on the product distribution of MTH reaction, it does not affect the dependence of coke on the deposition position.

In addition to the distribution of acidity and introduction of Zn, the third factor is that the diffusion of molecules through two kinds of pore channels is significantly different. According to previous studies

[44–46], the carbon species obtained by rapid polymerization between aromatics, such as toluene and TriMBs, have an obviously higher graphitization degree than those using C_2H_4 or C_3H_6 as carbon source under the same experimental conditions. These findings combined with our EELS results indicate that the diffusion paths of small molecules mainly are sinusoidal channels, while that of aromatics are straight channels (Fig. S10c) [47,48].

3.5. The statistics analysis for the preferred adsorption sites of product molecules

In order to prove this point, by using GCMC simulation [49], we perform a statistics analysis for the preferred adsorption sites of product molecules in the MFI framework under the reaction conditions. From

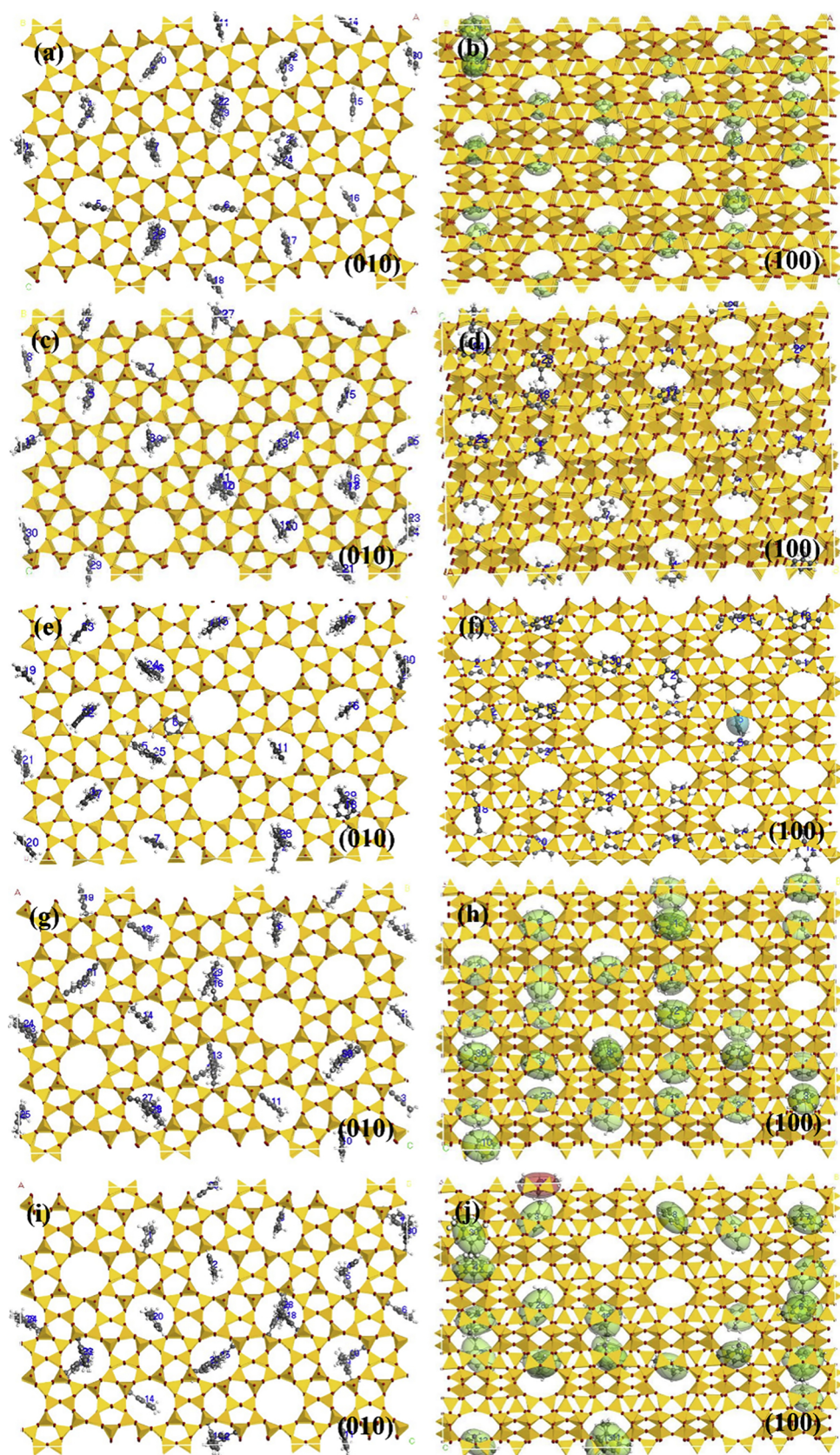


Fig. 10. The optimized location of (a,b) benzene, (c,d) toluene, (e,f) p-xylene, (g,h) o-xylene, and (i,j) m-xylene molecules along the straight and sinusoidal channels of the MFI zeolite.

Table 3

The adsorption probability distribution of product molecules in channels of MFI zeolite.

Product molecules	Position		
	sinusoidal channels	straight channels	channel intersections
C1 methane	15	11	4
C2 DME	16	13	1
ethylene	15	15	0
ethane	19	9	2
C3 propylene	16	13	1
propane	15	14	1
C4 cis-2-butene	16	14	0
trans-2-butene	17	12	1
n-butane	18	12	0
isobutane	0	26	4
butene	1	13	16
isobutene	2	23	5
C6 benzene	0	7	23
C7 toluene	0	20	10
C8 p-xylene	0	27	3
m-xylene	0	0	30
o-xylene	0	0	30
C9 1,2,3-TriMBs	0	0	30
1,2,4-TriMBs	0	0	30
1,3,5-TriMBs	0	0	30

Fig. 9 and Figs. S11–S14, we can observe that C₁–C₃, DME, cis²-butene, trans²-butene, and n-butane are small enough to travel randomly through the framework we built without diffusion limitations [50]. For isobutane, butene, isobutene, benzene, toluene, and p-xylene molecules, there fewer molecules being adsorbed in the sinusoidal channels (< 10%), while there are more in the straight channels and channel intersections (Figs. 9 and 10) because the jumps of these products along the sinusoidal channel structure occur at a much slower rate [51]. With the kinetic diameter of product molecules further increasing, more product molecules are adsorbed in the channel intersections. As the kinetic diameters of m-xylene, o-xylene, and TriMBs are larger than the diameters of pore channels, all m-xylene, o-xylene, and TriMBs molecules are adsorbed in channel intersections (Fig. 10 and Fig. S15). **Table 3** summarizes the adsorption probability distribution of all the product molecules in the sinusoidal channels, straight channels, and channel intersections of the MFI zeolite. According to these mechanics calculation results, it can be concluded that butene is the largest molecule which can diffuse in sinusoidal channels, while p-xylene is the largest molecule which can diffuse in straight channels. M-xylene, o-xylene, and TriMBs are too large to diffuse out of the pore channels of the MFI zeolite. Therefore, based on the above analysis, the reason for the significant difference of coke species (densities and sp^2/sp^3 ratios) between the (010) and (100) surfaces is that the diffusion of small molecule products occurs through both of the two channels, while aromatics are only diffused through the straight channels.

4. Conclusions

A series of Zn/ZSM-5 catalysts with various b-axis thickness (2–220 nm) were successfully synthesized by using different templates. The MTH reactions were systematically investigated over these Zn/ZSM-5 catalysts to elucidate the effect of b-axis thickness on their catalytic performance. The significant difference in diffusion distance along straight channel results in different product selectivities among these catalysts. As the intermediates of the aromatic-based cycle, MBs can easily diffuse out of the straight channels in Zn/ZSM-5 (2, 50), limiting the proportion of the aromatic-based cycle, while relatively promoting the olefin-based cycle. Consequently, Zn/ZSM-5 (2, 50) gives lower ethylene selectivity but higher TriMBs selectivity due to methylation reactions at the external surface, compared to samples with a

longer b-axis thickness. We have analyzed the coke species in the spent Zn/ZSM-5 (2, 50) catalysts and find that coke is preferentially formed in mesopores in the initial reaction period, and then mainly in micropores as the reaction proceeds. The distribution of coke over the deactivated Zn/ZSM-5 (2, 50) catalyst is concentrated on the (010) surface and is rare on the (100) surface, indicating that all product molecules diffuse out of Zn/ZSM-5 (2, 50) through the straight channels. EELS results show that coke residues over the (100) surface of Zn/ZSM-5 (60, 50) have a significantly different graphitization degree compared to that over the (010) surface. Combined with the adsorption simulations, we demonstrated that the diffusion of aromatics products is only through the straight channels. The largest product molecules which can diffuse in the sinusoidal and straight channels are butane and p-xylene, respectively.

Acknowledgements

This work is supported by the National Natural Science Foundation of China (21506111) and National Key R&D Program of China (2017YFB0602204 and 2018YFB0604803).

Appendix A. Supplementary data

Supplementary material related to this article can be found, in the online version, at doi:<https://doi.org/10.1016/j.apcatb.2018.11.023>.

References

- W. Song, D.M. Marcus, H. Fu, J.O. Ehresmann, J.F. Haw, An oft-studied reaction that may never have been: direct catalytic conversion of methanol or dimethyl ether to hydrocarbons on the solid acids HZSM-5 or HSAP-34, *J. Am. Chem. Soc.* 124 (2002) 3844–3845.
- D.M. McCann, D. Lesthaeghe, P.W. Kletnieks, D.R. Guenther, M.J. Hayman, V. van Speybroeck, M. Waroquier, J.F. Haw, A complete catalytic cycle for supramolecular methanol-to-olefins conversion by linking theory with experiment, *Angew. Chem. Int. Ed.* 47 (2008) 5179–5182.
- K. Shen, W. Qian, N. Wang, C. Su, F. Wei, Fabrication of c-axis oriented ZSM-5 hollow fibers based on an in situ solid–solid transformation mechanism, *J. Am. Chem. Soc.* 135 (2013) 15322–15325.
- Y. Li, M. Zhang, D. Wang, F. Wei, Y. Wang, Differences in the methanol-to-olefins reaction catalyzed by SAPO-34 with dimethyl ether as reactant, *J. Catal.* 311 (2014) 281–287.
- C. Wang, J. Xu, G. Qi, Y. Gong, W. Wang, P. Gao, Q. Wang, N. Feng, X. Liu, F. Deng, Methylbenzene hydrocarbon pool in methanol-to-olefins conversion over zeolite H-ZSM-5, *J. Catal.* 332 (2015) 127–137.
- B.T.W. Lo, L. Ye, G.G.Z. Chang, K. Purchase, S. Day, C.C. Tang, D. Mei, S.C.E. Tsang, Dynamic modification of pore opening of SAPO-34 by adsorbed surface methoxy species during induction of catalytic methanol-to-olefins reactions, *Appl. Catal. B* 237 (2018) 245–250.
- J.H. Ahn, B. Temel, E. Iglesia, Selective homologation routes to 2,2,3-trimethylbutane on solid acids, *Angew. Chem. Int. Ed.* 121 (2009) 3814–3816.
- D.A. Simonetti, J.H. Ahn, E. Iglesia, Mechanistic details of acid-catalyzed reactions and their role in the selective synthesis of triptane and isobutane from dimethyl ether, *J. Catal.* 277 (2011) 173–195.
- K. Shen, W. Qian, N. Wang, C. Su, F. Wei, Centrifugation-free and high yield synthesis of nanosized H-ZSM-5 and its structure-guided aromatization of methanol to 1, 2, 4-trimethylbenzene, *J. Mater. Chem. A* 2 (2014) 19797–19808.
- K. Shen, N. Wang, W. Qian, Y. Cui, F. Wei, Atmospheric pressure synthesis of nanosized ZSM-5 with enhanced catalytic performance for methanol to aromatics reaction, *Catal. Sci. Technol.* 4 (2014) 3840–3844.
- D. Masih, S. Rohani, J.N. Kondo, T. Tatsumi, Low-temperature methanol dehydration to dimethyl ether over various small-pore zeolites, *Appl. Catal. B* 217 (2017) 247–255.
- S. Kim, G. Park, S.K. Kim, Y.T. Kim, K.W. Jun, G. Kwak, Gd/HZSM-5 catalyst for conversion of methanol to hydrocarbons: effects of amounts of the Gd loading and catalyst preparation method, *Appl. Catal. B* 220 (2018) 191–201.
- S. Ilias, A. Bhan, Tuning the selectivity of methanol-to-hydrocarbons conversion on H-ZSM-5 by co-processing olefin or aromatic compounds, *J. Catal.* 290 (2012) 186–192.
- Z. Liu, X. Dong, Y. Zhu, A.H. Emwas, D. Zhang, Q. Tian, Y. Han, Investigating the influence of mesoporosity in zeolite beta on its catalytic performance for the conversion of methanol to hydrocarbons, *ACS Catal.* 5 (2015) 5837–5845.
- J. Zhu, Y. Cui, Y. Wang, F. Wei, Direct synthesis of hierarchical zeolite from a natural layered material, *Chem. Commun.* 22 (2009) 3282–3284.
- Z. Li, J. Martinez-Triguero, J. Yu, A. Corma, Conversion of methanol to olefins: stabilization of nanosized SAPO-34 by hydrothermal treatment, *J. Catal.* 329 (2015) 379–388.

[17] Z.M. Cui, Q. Liu, Z. Ma, S.W. Bian, W.G. Song, Direct observation of olefin homologations on zeolite ZSM-22 and its implications to methanol to olefin conversion, *J. Catal.* 258 (2008) 83–86.

[18] X.Y. Sun, S. Mueller, H. Shi, G.L. Haller, M. Sanchez-Sanchez, A.C. van Veen, J.A. Lercher, On the impact of co-feeding aromatics and olefins for the methanol-to-olefins reaction on HZSM-5, *J. Catal.* 314 (2014) 21–31.

[19] J. Zhu, Y. Zhu, L. Zhu, M. Rigutto, A. van der Made, C. Yang, S. Pan, L. Wang, L. Zhu, Y. Jin, Q. Sun, Q. Wu, X. Meng, D. Zhang, Y. Han, J. Li, Y. Chu, A. Zheng, S. Qiu, X. Zheng, F.S. Xiao, Highly mesoporous single-crystalline zeolite beta synthesized using a nonsurfactant cationic polymer as a dual-function template, *J. Am. Chem. Soc.* 136 (2014) 2503–2510.

[20] J.C. Kim, T.W. Kim, Y. Kim, R. Ryoo, S.Y. Jeong, C.U. Kim, Mesoporous MFI zeolites as high performance catalysts for Diels-Alder cycloaddition of bio-derived dimethylfuran and ethylene to renewable p-xylene, *Appl. Catal. B* 206 (2017) 490–500.

[21] A.A. Rownaghji, J. Hedlund, Methanol to gasoline-range hydrocarbons: influence of nanocrystal size and mesoporosity on catalytic performance and product distribution of ZSM-5, *Ind. Eng. Chem. Res.* 50 (2011) 11872–11878.

[22] R. Khare, D. Millar, A. Bhan, A mechanistic basis for the effects of crystallite size on light olefin selectivity in methanol-to-hydrocarbons conversion on MFI, *J. Catal.* 321 (2015) 23–31.

[23] N. Wang, W. Qian, K. Shen, C. Su, F. Wei, Bayberry-like ZnO/MFI zeolite as high performance methanol-to-aromatics catalyst, *Chem. Commun.* 52 (2016) 2011–2014.

[24] Y. Ni, A. Sun, X. Wu, G. Hai, J. Hu, T. Li, G. Li, The preparation of nano-sized H[Zn, Al]ZSM-5 zeolite and its application in the aromatization of methanol, *Microporous Mesoporous Mater.* 143 (2011) 435–442.

[25] G.T. Kokotailo, S.L. Lawton, D.H. Olson, W.M. Meier, Structure of synthetic zeolite ZSM-5, *Nature* 272 (1978) 437–438.

[26] D.H. Olson, G.T. Kokotailo, S.L. Lawton, W.M. Meier, Crystal structure and structure-related properties of ZSM-5, *J. Phys. Chem.* 85 (1981) 2238–2243.

[27] K. Na, C. Jo, J. Kim, K. Cho, J. Jung, Y. Seo, R.J. Messinger, B.F. Chmelka, R. Ryoo, Directing zeolite structures into hierarchically nanoporous architectures, *Science* 333 (2011) 328–332.

[28] X. Zhu, L. Wu, P.C.M.M. Magusin, B. Mezari, E.J.M. Hensen, On the synthesis of highly acidic nanolayered ZSM-5, *J. Catal.* 327 (2015) 10–21.

[29] Q. Tian, Z. Liu, Y. Zhu, X. Dong, Y. Saini, J.M. Basset, M. Sun, W. Xu, L. Zhu, D. Zhang, J. Huang, X. Meng, F.S. Xiao, Y. Han, Beyond creation of mesoporosity: the advantages of polymer-based dual-function templates for fabricating hierarchical zeolites, *Adv. Funct. Mater.* 26 (2016) 1881–1891.

[30] Y. Lou, P. He, L. Zhao, W. Cheng, H. Song, Olefin upgrading over Ir/ZSM-5 catalysts under methane environment, *Appl. Catal. B* 201 (2017) 278–289.

[31] Y. Wang, J. Song, N.C. Baxter, G.T. Kuo, S. Wang, Synthesis of hierarchical ZSM-5 zeolites by solid-state crystallization and their catalytic properties, *J. Catal.* 349 (2017) 53–65.

[32] J. Ding, P. Chen, G. Zhao, Y. Liu, Y. Lu, High-performance thin-felt SS-fiber@HZSM-5 catalysts synthesized via seed-assisted vapor phase transport for methanol-to-propylene reaction: effects of crystal size, mesoporosity and aluminum uniformity, *J. Catal.* 360 (2018) 40–50.

[33] E. Soghrati, T.K.C. Ong, C.K. Poh, S. Kawi, A. Borgna, Zeolite-supported nickel phyllosilicate catalyst for CeO₂ hydrogenolysis of cyclic ethers and polyols, *Appl. Catal. B* 235 (2018) 130–142.

[34] J. Kim, M. Choi, R. Ryoo, Effect of mesoporosity against the deactivation of MFI zeolite catalyst during the methanol-to-hydrocarbon conversion process, *J. Catal.* 269 (2010) 219–228.

[35] T.V.W. Janssens, A new approach to the modeling of deactivation in the conversion of methanol on zeolite catalysts, *J. Catal.* 264 (2009) 130–137.

[36] H. Schulz, “Coking” of zeolites during methanol conversion: basic reactions of the MTO-, MTP- and MTG processes, *Catal. Today* 154 (2010) 183–194.

[37] J. Abbot, B.W. Wojciechowski, Catalytic reactions of n-hexenes on amorphous silica-alumina, *Can. J. Chem. Eng.* 63 (1985) 818–825.

[38] D. Rojo-Gama, M. Signorile, F. Bonino, S. Bordiga, U. Olsbye, K.P. Lillerud, P. Beato, S. Svelle, Structure-deactivation relationships in zeolites during the methanol-to-hydrocarbons reaction: complementary assessments of the coke content, *J. Catal.* 351 (2017) 33–48.

[39] C. Duong-Viet, Y. Liu, H. Ba, L. Truong-Phuoc, W. Baaziz, L. Nguyen-Dinh, J.M. Nhut, C. Pham-Huu, Carbon nanotubes containing oxygenated decorating defects as metal-free catalyst for selective oxidation of H₂S, *Appl. Catal. B* 191 (2016) 29–41.

[40] R.J. Klein, D.A. Fischer, J.L. Lenhart, Systematic oxidation of polystyrene by ultraviolet-ozone, characterized by near-edge X-ray absorption fine structure and contact angle, *Langmuir* 24 (2008) 8187–8197.

[41] S. Urbonaite, S. Wachtmeister, C. Murguet, E. Coronel, W.Y. Zou, S. Csillag, G. Svensson, EELS studies of carbide derived carbons, *Carbon* 45 (2007) 2047–2053.

[42] J.E. Schmidt, J.D. Poplawsky, B. Mazumder, Ö. Attila, D. Fu, D.A.M. de Winter, F. Meirer, S.R. Bare, B.M. Weckhuysen, Coke formation in a zeolite crystal during the methanol-to-hydrocarbons reaction as studied with atom probe tomography, *Angew. Chem. Int. Ed.* 55 (2016) 11173–11177.

[43] I. Pinilla-Herrero, E. Borfecchia, J. Holzinger, U.V. Mentzel, F. Joensen, K.A. Lomachenko, S. Bordiga, C. Lamberti, G. Berlier, U. Olsbye, S. Svelle, J. Skibsted, P. Beato, High Zn/Al ratios enhance dehydrogenation vs hydrogen transfer reactions of Zn-ZSM-5 catalytic systems in methanol conversion to aromatics, *J. Catal.* 362 (2018) 146–163.

[44] A.M. Benito, Y. Maniette, E. Muñoz, M.T. Martínez, Carbon nanotubes production by catalytic pyrolysis of benzene, *Carbon* 36 (1998) 681–683.

[45] Y. Yang, Z. Hu, Y.J. Tian, Y.N. Lü, X.Z. Wang, Y. Chen, High-yield production of quasi-aligned carbon nanotubes by catalytic decomposition of benzene, *Nanotechnology* 14 (2003) 733–737.

[46] T. Iguchi, S. Takenaka, K. Nakagawa, Y. Orita, H. Matsune, M. Kishida, Production of carbon nanotube by ethylene decomposition over silica-coated metal catalysts, *Top. Catal.* 52 (2009) 563–570.

[47] D. Mores, J. Kornatowski, U. Olsbye, B.M. Weckhuysen, Coke formation during the methanol-to-olefin conversion: in situ microspectroscopy on individual H-ZSM-5 crystals with different Brønsted acidity, *Chem. Eur. J.* 17 (2011) 2874–2884.

[48] J.P. Hofmann, D. Mores, L.R. Aramburo, S. Teketel, M. Rohnke, J. Janek, U. Olsbye, B.M. Weckhuysen, Large zeolite H-ZSM-5 crystals as models for the methanol-to-hydrocarbons process: bridging the gap between single-particle examination and bulk catalyst analysis, *Chem. Eur. J.* 19 (2013) 8533–8542.

[49] G. Vella, G.E. Imoberdorf, A. Sclafani, A.E. Cassano, O.M. Alfano, L. Rizzuti, Modeling of a TiO₂-coated quartz wool packed bed photocatalytic reactor, *Appl. Catal. B* 96 (2010) 399–407.

[50] J. Kärger, Random walk through two-channel networks: a simple means to correlate the coefficients of anisotropic diffusion in ZSM-5 type zeolites, *J. Phys. Chem.* 95 (1991) 5558–5560.

[51] R. Krishna, J.M. van Baten, E. García-Pérez, S. Calero, Diffusion of CH₄ and CO₂ in MFI, CHA and DDR zeolites, *Chem. Phys. Lett.* 429 (2006) 219–224.